Supplemental Material for Spin-fluctuation-induced pairing in twisted bilayer graphene

Ammon Fischer,[1] Lennart Klebl,[2] Carsten Honerkamp,[1] and Dante M. Kennes[2,3]

[1] *Institute for Theoretical Solid State Physics, RWTH Aachen University, and JARA Fundamentals of Future Information Technology, 52062 Aachen, Germany*
[2] *Institute for Theory of Statistical Physics, RWTH Aachen University, and JARA Fundamentals of Future Information Technology, 52062 Aachen, Germany*
[3] *Max Planck Institute for the Structure and Dynamics of Matter, Center for Free Electron Laser Science, 22761 Hamburg, Germany*

S I. ATOMIC STRUCTURE OF TWISTED BILAYER GRAPHENE

The atomic structure of twisted bilayer graphene (TBG) consists of two super-imposed graphene layers rotated by an angle θ and separated by a distance of $d_0 = 0.335$ nm. The axis of rotation is chosen to intersect two vertically aligned carbon atoms when starting from purely AA-stacked bilayer, i.e. two perfectly overlapping honeycomb lattices. Labelling the upper (lower) monolayer of TBG by $u(l)$, their two-dimensional lattice vectors are

$$\begin{aligned} \boldsymbol{a}_1^l &= a_0(\cos(\pi/6), -\sin(\pi/6)) \\ \boldsymbol{a}_2^l &= a_0(\cos(\pi/6), \ \ \sin(\pi/6)) \\ \boldsymbol{a}_i^u &= R(\theta)\boldsymbol{a}_i^l, \end{aligned} \tag{1}$$

where $R(\theta)$ represents a rotation by an angle θ and $a_0 = 0.246\,\text{nm}$ is the lattice constant of graphene, which should not be confused with the carbon-carbon bond length of $a_{\text{cc}} = a_0/\sqrt{3}$. The so defined primitive cell is di-atomic and contains two inequivalent sites with basis vectors

$$\begin{aligned} \boldsymbol{b}_1^{u(l)} &= (0,0) && \text{(A site)}, \\ \boldsymbol{b}_2^{u(l)} &= \frac{1}{3}\boldsymbol{a}_1^{u(l)} + \frac{1}{3}\boldsymbol{a}_2^{u(l)} && \text{(B site)}. \end{aligned} \tag{2}$$

The choice of basis vectors and the type of rotation around an AA site restricts the symmetry of TBG to point group D_3. The latter contains a threefold in-plane rotation $C_3 = C_{3z}$ around the z-axis and a twofold out-of-plane rotation $C_2 = C_{2y}$.
The lattice geometry of TBG, as defined so far, is not periodic in general [1–3] since the periods of the two graphene layers are incommensurate for arbitrary twist angles. A finite unit cell can only be constructed for some discrete angles satisfying the condition

$$\cos(\theta) = \frac{1}{2}\frac{m^2+n^2+mn}{m^2+n^2+mn} \tag{3}$$

with (m,n) being positive integers. In this case, the twisted bilayer graphene forms a moiré pattern, see Fig. 1 (a), containing $N(m,n) = 4(m^2+n^2+mn)$ atoms with superlattice vectors

$$\begin{aligned} \boldsymbol{L}_1 &= m\boldsymbol{a}_1^l + n\boldsymbol{a}_2^l = n\boldsymbol{a}_1^u + m\boldsymbol{a}_2^u \\ \boldsymbol{L}_2 &= R(\pi/3)\boldsymbol{L}_1. \end{aligned} \tag{4}$$

Magic-angle twisted bilayer graphene has a twist angle of $\theta = 1.05^\circ$ corresponding to the the integers $(m,n) = (31,32)$. The so defined structure contains $N = 11908$ carbon atoms in the moiré unit cell. When discussing the geometric structure of TBG, atomic relaxation effects play an important role and may modify the low-energy physics of the system significantly. From experiments using transmission electron microscopy (TEM) [4] as well as from structural optimization studies using density functional theory [5] it is known that the interlayer distance between the two layers varies over the moiré unit cell. The interlayer spacing takes its maximum value $d_{AA} = 0.360\,\text{nm}$ in the AA regions and its minimal value $d_{AB} = 0.335\,\text{nm}$ in the AB regions. Intermediate spacings $d(\boldsymbol{r})$ are obtained by using an interpolation suggested by [1, 5]

$$d(\boldsymbol{r}) = d_0 + 2d_1\sum_{i=1}^{3}\cos\left(\boldsymbol{G}_i\cdot\boldsymbol{r}\right), \tag{5}$$

where the vector $\boldsymbol{r}$ points to a carbon atom in the moiré unit cell and $\boldsymbol{G}$ are the reciprocal lattice vectors obtained from Eq. (4). Furthermore, the constants $d_0 = \frac{1}{3}(d_{AA} + 2d_{AB})$ and $d_1 = \frac{1}{9}(d_{AA} - d_{AB})$ are defined such to match the distances in the AA and AB regions. In order to preserve the D_3 symmetry of the system, the corrugation must be applied symmetric to both layers as depicted in Fig. 1 (c).

S II. ATOMISTIC TIGHT-BINDING HAMILTONIAN

The eigenenergies and eigenfunctions of non-interacting TBG are obtained using a single-orbital tight-binding Hamiltonian for the p_z-orbitals of the

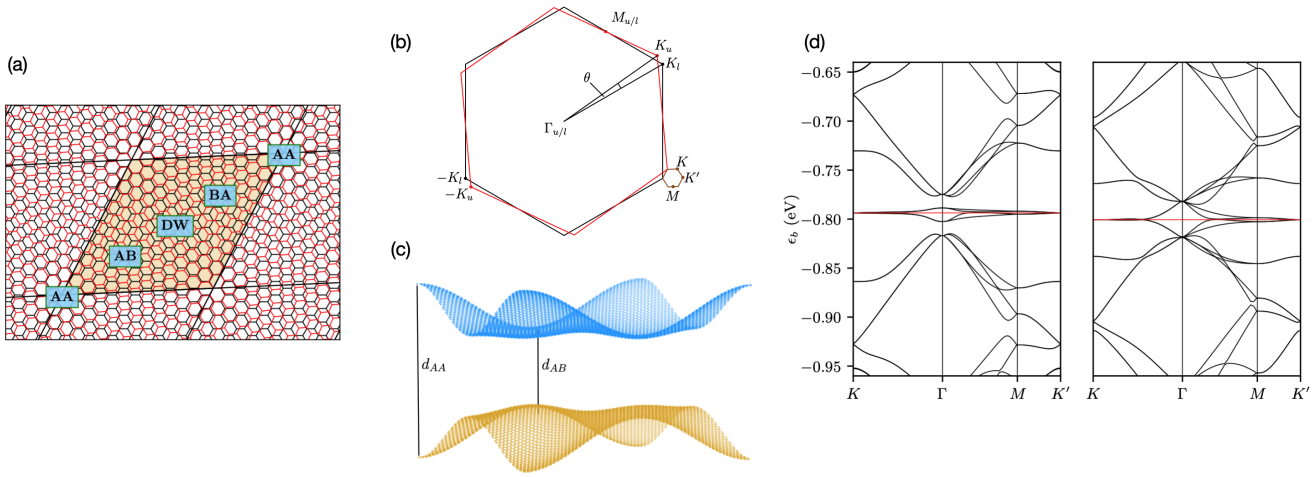

Figure 1. **Atomic structure of twisted bilayer graphene. (a)** Atomic structure of twisted bilayer graphene with twist angle $\theta = 5.09^\circ$ corresponding to $(m, n) = (6, 7)$. The blue labels indicate characteristic stacking patterns emerging throughout the moiré unit cell. **(b)** Downfolding of the (mini-) Brillouin zone of TBG (brown hexagon). **(c)** Corrugation effects in TBG. **(d)** Band structure of magic-angle TBG with twist angle $\theta = 1.05^\circ$ corresponding to $(m, n) = (31, 32)$. The low-energy window around charge neutrality (red line) is modified significantly when corrugation of the two graphene sheets is taken into account (left panel). This is reflected in the formation of four flat bands (two-fold spin degeneracy) around charge neutrality that have a bandwidth of $\approx 15\,\text{meV}$ and are separated from the rest of the spectrum.

carbon atoms [1, 2, 6]:

$$H = \sum_{\boldsymbol{R},\boldsymbol{R}'} \sum_{i,j,\sigma} t(\boldsymbol{R} + \boldsymbol{r}_i - \boldsymbol{R}' - \boldsymbol{r}_j) c^\dagger_{\boldsymbol{R},\boldsymbol{r}_i,\sigma} c_{\boldsymbol{R}',\boldsymbol{r}_j,\sigma}. \quad (6)$$

For our microscopic approach we account for the full π-band spectrum of magic-angle TBG, keeping all $N = 11908$ bands under consideration. In the following, we label the supercell vector with $\boldsymbol{R}$ and the position vector of site i in the corresponding moiré unit cell with $\boldsymbol{r}_i$. Hence, the operator $c^\dagger_{\boldsymbol{R},\boldsymbol{r}_i,\sigma}$ creates an electron with spin $\sigma = \uparrow, \downarrow$ in the p_z-orbital of site i, whereas $c_{\boldsymbol{R},\boldsymbol{r}_i,\sigma}$ destroys an electron with the same quantum numbers. The transfer integral between orbitals at site i and j, separated by the vector $\boldsymbol{d}$ can be written in Slater-Koster form [1]

$$\begin{aligned} t(\boldsymbol{d}) &= t_\parallel(\boldsymbol{d}) + t_\perp(\boldsymbol{d}) \\ t_\parallel(\boldsymbol{d}) &= -V^0_{pp\pi} \exp\left(-\frac{d - a_{\text{cc}}}{\delta_0}\right)\left[1 - \left(\frac{d^z}{d}\right)^2\right] \\ t_\perp(\boldsymbol{d}) &= -V^0_{pp\sigma} \exp\left(-\frac{d - d_0}{\delta_0}\right)\left[\frac{d^z}{d}\right]^2. \end{aligned} \quad (7)$$

Here, $d^z = \boldsymbol{d} \cdot \boldsymbol{e}_z$ points perpendicular to the graphene sheets and $d_0 = 1.362\,a_0$ is the vertical spacing of graphite. The term $V_{pp\sigma} = 0.48$ eV describes the interlayer hopping between atoms in different monolayers of TBG, while $V_{pp\pi} = -2.7$ eV models the intralayer hopping amplitude between neighboring atoms in a single graphene sheet. The parameters are fitted to data of first principle calculations to match the dispersion of mono- and bilayer graphene [1]. This ensures in particular that TBG behaves locally similar to graphene with the overall structure being modulated by the moiré pattern. The parameter $\delta_0 = 0.184\,a_0$ determines the decay length of the transfer integral and is chosen such that the nearest-neighbor intralayer hopping reduces to $0.1 V_{pp\pi}$. For numerical calculations it is therefore sufficient to truncate hopping terms for $r_{ij} > 4\,a_0$ as $t(\boldsymbol{r}_{ij}) < 10^{-4}$ in these regimes.

To construct the full non-interacting Hamiltonian of the periodic system, we define the Bloch wave basis by a Fourier transform to mini-Brillouin zone (MBZ) momentum $\boldsymbol{k}$, which is depicted in Fig. 1 (b),

$$\begin{aligned} c_{\boldsymbol{k},\boldsymbol{r}} &= \frac{1}{\sqrt{N}} \sum_{\boldsymbol{R}} e^{i\boldsymbol{k}\boldsymbol{R}} c_{\boldsymbol{R},\boldsymbol{r}} \\ c_{\boldsymbol{R},\boldsymbol{r}} &= \frac{1}{\sqrt{N}} \sum_{\boldsymbol{k}} e^{-i\boldsymbol{k}\boldsymbol{R}} c_{\boldsymbol{k},\boldsymbol{r}}. \end{aligned} \quad (8)$$

The spin index is omitted for simplicity. Note that the moiré Fourier transform as defined above couples momenta $\boldsymbol{k}$ and superlattice vectors $\boldsymbol{R}$. The latter describe the spatial extent of the moiré unit cell, which in the case of magic-angle TBG is given by $L = |\boldsymbol{L}_{1,2}| = 13.42\,\text{nm}$.

Inserting these expressions into Eq.(6) renders the unperturbed Hamiltonian block-diagonal in momentum

space

$$H_0 = \sum_{\boldsymbol{k}} \sum_{\boldsymbol{R}-\boldsymbol{R}'} \sum_{i,j,\sigma} t(\boldsymbol{R}+\boldsymbol{r}_i-\boldsymbol{R}'-\boldsymbol{r}_j) \times e^{-i\boldsymbol{k}\cdot(\boldsymbol{R}-\boldsymbol{R}')} c^\dagger_{\boldsymbol{k},\boldsymbol{r}_i,\sigma} c_{\boldsymbol{k},\boldsymbol{r}_j,\sigma} \quad (9)$$
$$= \sum_{\boldsymbol{k}} \sum_{i,j,\sigma} [H_0(\boldsymbol{k})]_{\boldsymbol{r}_i,\boldsymbol{r}_j} c^\dagger_{\boldsymbol{k},\boldsymbol{r}_i,\sigma} c_{\boldsymbol{k},\boldsymbol{r}_j,\sigma}.$$

The matrix $[H_0(\boldsymbol{k})]_{\boldsymbol{r}_i,\boldsymbol{r}_j}$ can be diagonalized in orbital space (i,j) for each $\boldsymbol{k}$ to obtain the bandstructure $\epsilon_b(\boldsymbol{k})$ and orbital-to-band transformation $u^b_{\boldsymbol{r}}(\boldsymbol{k})$, $b = 1..N$:

$$H_0 = \sum_{\boldsymbol{k},b} \epsilon_b(\boldsymbol{k}) \gamma^\dagger_{\boldsymbol{k},b} \gamma_{\boldsymbol{k},b} \qquad \text{with} \quad \gamma_{\boldsymbol{k},b} = u^b_{\boldsymbol{r}}(\boldsymbol{k}) c_{\boldsymbol{k},\boldsymbol{r}}. \quad (10)$$

Since magic-angle TBG contains $N = 11908$ atoms in the moiré unit cell, care must be taken when treating the system numerically.

S III. MAGNETIC INSTABILITIES AND STONER CRITERION

A. Stoner Criterion

In the manuscript, we study magnetic instabilities in TBG described by short-ranged Coulomb interactions. To this end, we follow Ref. [7] and employ a repulsive Hubbard term for electrons with opposite spin σ with $\overline{\sigma} = -\sigma$ residing on the same carbon site

$$H_{\text{int}} = \frac{1}{2} U \sum_{\boldsymbol{R},i,\sigma} n_{\boldsymbol{R},\boldsymbol{r}_i,\sigma} n_{\boldsymbol{R},\boldsymbol{r}_i,\overline{\sigma}}. \quad (11)$$

To treat the interacting system in a pertubative manner, we define the free Matsubara Green's function in orbital-momentum space as

$$g_{\boldsymbol{r},\boldsymbol{r}'}(i\omega,\boldsymbol{k}) = \sum_b u^b_{\boldsymbol{r}}(\boldsymbol{k}) (i\omega - e_b(\boldsymbol{k}))^{-1} u^{b*}_{\boldsymbol{r}'}(\boldsymbol{k}). \quad (12)$$

We then calculate the renormalized interaction in the spin channel within the random-phase approximation (RPA) to analyze the electronic instabilities mediated by spin-fluctuation exchange between electrons to high order in the bare coupling U. Since the initial short-ranged interaction vertex U has no momentum and frequency dependence, the full susceptibility of the system can be approximated by $\hat{\chi}^{\text{RPA}}(q) = \hat{\chi}_0(q)/[1 + U\hat{\chi}_0(q)]$. Here, we use the multi-index qunatum number $q = (\boldsymbol{q}, i\omega)$ and indicate matrices of dimension $N \times N$ with an hat symbol, e.g. $\hat{\chi} = \chi_{\boldsymbol{r},\boldsymbol{r}'}$. Magnetic instabilities may subsequently be classified according to a generalized Stoner criterion: The effective (RPA) interaction diverges, when the smallest eigenvalue λ_0 of $\hat{\chi}(q)$ reaches $-1/U$, marking the onset of magnetic order for all interaction strengths $U \geq U_{\text{crit.}} = -1/\lambda_0$. The corresponding eigenvector $v^{(0)}(q)$ is expected to dominate the spatial structure of orbital magnetization.

In this letter, we study magnetic instabilities with emphasis on the static, long-wavelength limit $(\boldsymbol{q}, i\omega \to 0)$ on the moiré scale. The latter limit proves to contain the relevant physics when starting with local repulsive interaction. We stress again that momenta $\boldsymbol{q}$ are related via moiré Fourier transform Eq. (8) to the superlattice vectors $\boldsymbol{R}$. The RPA susceptibility predicts spin correlations at length scales intermediate to the c-c bond scale and moiré length scale, thus being described by orderings at $\boldsymbol{q} = 0$. The system shows the same order in all moiré unit cells with variable correlations present on the c-c bond scale.

B. Spin susceptibility

For analyzing the magnetic properties of the system on the RPA level, it is therefore sufficient to compute the free polarization function $\hat{\chi}_0(q)$ defined as

$$\chi_{0_{\boldsymbol{r},\boldsymbol{r}'}}(\boldsymbol{q}, i\omega) = \frac{1}{N\beta} \sum_{\boldsymbol{k},\omega'} g_{\boldsymbol{r},\boldsymbol{r}'}(i\omega', \boldsymbol{k}) g_{\boldsymbol{r}',\boldsymbol{r}}\left(i(\omega'+\omega), \boldsymbol{k}+\boldsymbol{q}\right). \quad (13)$$

The Matsubara summation occuring in Eq. (13) can be evaluated analytically yielding the well-known Lindhard function for multi-orbital systems

$$\chi_{0_{\boldsymbol{r},\boldsymbol{r}'}}(\boldsymbol{q}, i\omega) = \frac{1}{N} \sum_{\boldsymbol{k},b,b'} \frac{n_F(\epsilon_{b'}(\boldsymbol{k})) - n_F(\epsilon_b(\boldsymbol{k}+\boldsymbol{q}))}{i\omega + \epsilon_{b'}(\boldsymbol{k}) - \epsilon_b(\boldsymbol{k}+\boldsymbol{q})} \times u^{b'}_{\boldsymbol{r}}(\boldsymbol{k}) u^{b'*}_{\boldsymbol{r}'}(\boldsymbol{k}) u^{b*}_{\boldsymbol{r}}(\boldsymbol{k}+\boldsymbol{q}) u^{b}_{\boldsymbol{r}'}(\boldsymbol{k}+\boldsymbol{q}), \quad (14)$$

where $n_F(\epsilon) = (1 + e^{\beta\epsilon})^{-1}$ is the Fermi function. While the analytical evaluation of the Matsuabra sum occuring in Eq. (13) is the standard procedure for systems containing only few atoms in the unit cell, this approach is destined to fail in our atomistic approach as it scales like $\mathcal{O}(N^4)$. For magic-angle TBG with $N = 11908$ atoms in the moiré unit cell, it is more efficient to compute the Matsubara sum in Eq. (13) numerically over a properly chosen frequency grid and in each step compute Hadamard products of band-summed non-local Green's functions $g_{\boldsymbol{r},\boldsymbol{r}'}(i\omega', \boldsymbol{k}) g^T_{\boldsymbol{r},\boldsymbol{r}'}\left(i(\omega'+\omega), \boldsymbol{k}+\boldsymbol{q}\right)$. The expression then scales like $\mathcal{O}(N^3 N_\omega)$ with N_ω being the number of fermionic frequencies needed to achieve proper convergence. To this end, non-linear mixing schemes [8] are proven to outperform any linear summation such that we only need to sum over $N_\omega \approx 1000$ frequencies when accessing temperatures down to $T = 0.03\,\text{meV}$. The momentum sum occuring in Eq. (13) is evaluated over 24 $\boldsymbol{k}$ points in the MBZ using a momentum meshing proposed by Cunningham et al. [9]. In particular, we checked

that the results are sufficiently converged when taking an denser mesh into account.

C. Leading Instabilities

In the manuscript, we classify the different leading eigenvectors of the RPA analysis according to their real-space profile in the moiré unit cell following the nomenclature introduced in Ref. [7]. The three potential ground states of the interacting system at $T = 0.03\,\mathrm{meV}$ are depicted in Fig. 2 (b): (i) AFM: moiré-modulated antiferromagnetic phase on the carbon-carbon bond scale ("Ångström"-scale) with increased weight in the AA regions, (ii) DAFM: moiré-modulated antiferromagnetic phase with opposite signs between the AA and AB regions that becomes visible as a node in the absolute value of the order parameter, (iii) FM: moiré-modulated ferromagnetic phase (FM) that exhibits the same overall sign in the moiré unit cell. The choice of the temperature $T = 0.03\,\mathrm{meV}$ should provide resolution of the flat energy bands in TBG as extensively discussed in Ref. [7]. As long as $T \gg \mathcal{O}(1\,\mathrm{meV})$ the flat band physics is not resolved and the system inherits magnetic order from purely AA and AB stacked bilayer graphene. For $T \approx \mathcal{O}(1\,\mathrm{meV}) \approx 10\,\mathrm{K}$, significant deviations due to the flat bands occur, leading to the plethora of magnetic phases described above.

S IV. SELF-CONSISTENT BOGOLIUBOV DE-GENNES EQUATIONS FOR TBG

A. Fluctuation-Exchange approximation

For interaction values $U < U_{\mathrm{crit}}$ the system is in the paramagnetic regime and the magnetic instabilities prescribed by the RPA analysis are not strong enough to actually occur. In this regime, spin and charge fluctuations contained in the transverse and longitudinal spin channel can give rise to an effective interaction between electrons that may lead to the formation of Cooper pairs. The leading RPA diagrams to the irreducible singlet particle-particle scattering vertex $\hat{\Gamma}_2(\boldsymbol{q}, \nu)$ are captured within the fluctuations-exchange approximation (FLEX) [10, 11]

$$\hat{\Gamma}_2(\boldsymbol{q}) = \hat{U} - \frac{U^2\hat{\chi}_0(\boldsymbol{q})}{1 + U\hat{\chi}_0(\boldsymbol{q})} + \frac{U^3\hat{\chi}_0^2(\boldsymbol{q})}{1 - U^2\hat{\chi}_0^2(\boldsymbol{q})}. \tag{15}$$

As in the previous section, we only consider the static long-wavelength limit $(\boldsymbol{q}, i\omega \to 0)$ and thus focus on the pairing structure on the carbon-carbon bonds within the moiré unit cell. To this end, the real-space profile of the effective interaction $\hat{\Gamma}_2$ for different chemical potentials is shown in Fig. 2 (c). As mentioned in the manuscript, the interaction vertex is staggered through the moiré unit cell close to a DAFM/AFM instability, opening the door for unconventional singlet Cooper pairs in the two graphene sheets of TBG. In particular, the interlayer interaction strength is an order of magnitude smaller than comparable intralayer terms. This indicates that the main pairing will create in-plane Cooper pairs. In the manuscript, we thus only visualize the projection of the superconducting order parameters on the in-plane form factor basis of each graphene sheet, i.e. a layer-resolved representation.

B. Self-consistent BdG Formalism

In the next step, we analyze the effective particle-particle scattering vertex Eq. (15) using a mean-field decoupling to extract pairing symmetries and spatial distribution of the superconducting order parameter. In the static long-wavelength limit $(\boldsymbol{q}, i\omega \to 0)$, we may hence neglect the momentum dependence of the gap parameter and effectively solve a one-unit cell system with periodic boundary conditions. While this approach does not take correlations between different moiré unit cells into account, it allows for all pairing contributions from within the moiré unit cell. Due to the proximity to the antiferromagnetic ordered state, we restrict the mean-field decoupling to spin-singlet configurations that are symmetric under the exchange of spatial indices

$$\Delta_{ij} = -\frac{1}{2}\left[\Gamma_2(q=0)\right]_{ij}\langle c_{i\uparrow}c_{j\downarrow} - c_{i\downarrow}c_{j\uparrow}\rangle_{\mathrm{MF}}. \tag{16}$$

The expectation value $\langle\cdot\rangle_{\mathrm{MF}}$ can be calculated by diagonalizing the resulting mean-field Hamiltonian H_{MF} in Nambu-space using a Bogoliubov de-Gennes transformation [12]

$$\begin{aligned} H_{\mathrm{MF}} &= \psi^\dagger \begin{pmatrix} \hat{H}_0 & \hat{\Delta} \\ \hat{\Delta}^\dagger & -\hat{H}_0 \end{pmatrix} \psi \\ \langle c_{i\uparrow}c_{j\downarrow} - c_{i\downarrow}c_{j\uparrow}\rangle_{\mathrm{MF}} &= \sum_n \left(u_i^n v_j^{n*} + u_j^n v_i^{n*}\right) \tanh\left(\frac{E^n}{2T}\right). \end{aligned} \tag{17}$$

Here, u_i^n (v_i^n) are the particle (hole) amplitudes of the BdG quasi-particles resulting from the diagonalization of the Hamiltonian in Eq. (17)

$$\begin{aligned} H_{\mathrm{MF}} &= \left(\hat{U}\psi\right)^\dagger \begin{pmatrix} \hat{E} & 0 \\ 0 & -\hat{E} \end{pmatrix} \left(\hat{U}\psi\right) \\ \hat{U} &= \begin{pmatrix} \hat{u} & \hat{v} \\ -\hat{v}^* & \hat{u} \end{pmatrix}, \end{aligned} \tag{18}$$

and $\psi = (c_{1\uparrow}, ..., c_{N\uparrow}, c_{1\downarrow}^\dagger, ..., c_{N\downarrow}^\dagger)^T$ is the $2N$-component Nambu vector. $\sum_n$ denotes a sum over the positive quasi-particle energies $E_n > 0$ and $\hat{E}$ is the corresponding diagonal matrix. To solve this set of self-consistent equa-

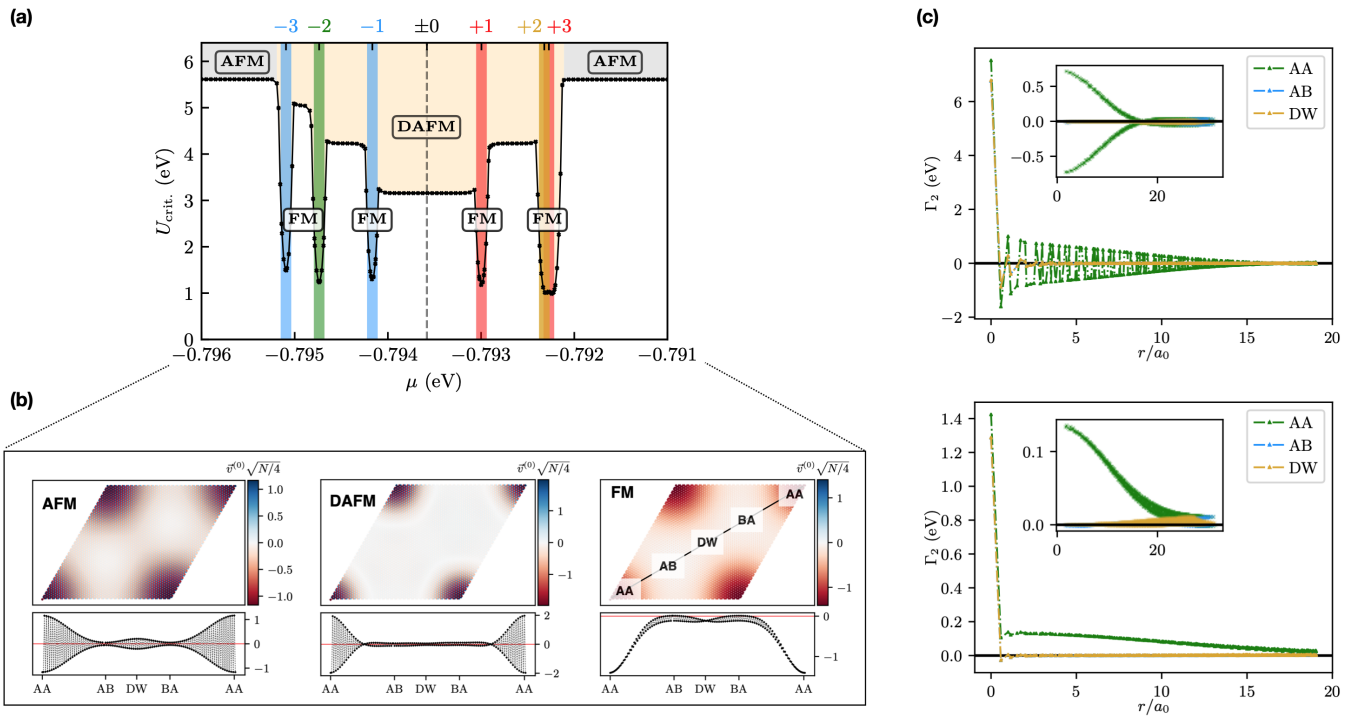

Figure 2. Spin correlations in magic-angle TBG. (a) Magnetic RPA phase diagram showing the critical onsite interaction strength $U_{\mathrm{crit.}}$ vs. chemical potential μ in the four flat bands of TBG at $T = 0.03\,\mathrm{meV}$. The vertical lines indicate the integer fillings $\pm 3, \pm 2, \pm 1$ that show an increased magnetic ordering tendency towards a moiré-modulated ferromagnetic state, while away from integer fillings weaker antiferromagnetic tendencies dominate. **(b)** Spatial distribution of the leading eigenvector of the RPA analysis on the carbon-carbon bond scale in the moiré unit cell. For simplicity, only the lower layer of TBG is shown as well as a linecut through the unit cell. The leading eigenvector of the DAFM instabilities is staggered throughout the moiré unit cell with strongest weight in the AA regions as depicted in the linecut in (b). **(c)** Effective spin-fluctuation mediated pairing vertex $\Gamma_2(q = 0)$ close to a DAFM (upper panel) and FM (lower panel) magnetic instability. In the former case, the pairing vertex is staggered in real-space with strong on-site repulsion and nearest-neighbor attraction. Real-space profiles are shown starting from an atom located in the AA, AB or DW region of TBG, respectively.

tions we start with an initial guess for Δ_{ij} and iterate until convergence is achieved using a linear mixing scheme to avoid any bipartite solutions. Since the atomic arrangement is highly inhomogeneous in the moiré unit cell, we track the free energy during each self-consistency cycle and for different initial configurations to ensure proper convergence of the algorithm into the actual global minimum. The free energy of the system in the low temperature regime reads

$$F = E - TS \approx E_g - \sum_n E_n - \sum_{ij} \frac{|\Delta_{ij}|^2}{\Gamma_{2,ij}} \tag{19}$$

where $E_g = 2\sum_n E_n n_F(E_n)$ is the excitation energy of the quasi-particles. The different initial configurations are chosen to transform according to the irreducible representations of the D_{6h} point group of the honeycomb lattice. This procedure aligns with the insights from the previous paragraph that the spin-fluctuation mediated pairing vertex Eq. (15) will create in-plane Cooper pairs with strongest pairing amplitude living on the nearest-neighbor bonds of the two single graphene sheets. The phase factors of the different nearest-neighbor pairing channels are shown in Fig. 3.

C. Supercurrent and magnetic field

To characterize the different superconducting phases of the system, we compute the layer resolved quasi-particle bond current in TBG [12]

$$\boldsymbol{J}_{nm} = \frac{e}{i\hbar}\langle c_n^\dagger t_{nm} c_m - c_m^\dagger t_{mn} c_n\rangle \hat{\boldsymbol{e}}_{nm}. \tag{20}$$

In the atomistic approach presented here, the quasi-particle current $\boldsymbol{J}_{nm}$ is only defined between two carbon atoms residing at sites $\boldsymbol{r}_{n(m)}$ in the moiré unit cell. Therefore, we take an amplitude-weighted average of neighboring bonds to arrive at a vector field represen-

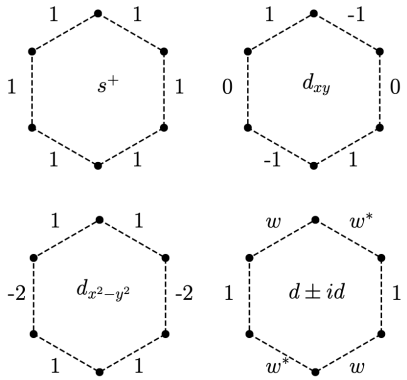

Figure 3. Form factors for different nearest-neighbor (singlet) pairing channels on the honeycomb lattice. The complex linear combination $d \pm id$ is characterized by the phase factor $w = \exp(\pm i\, 2\pi/3)$.

tation $\boldsymbol{J}$ as shown in Fig. 3 in the manuscript

$$\boldsymbol{J}(\boldsymbol{r}_n) = \frac{1}{3} \sum_{\langle m \rangle} \boldsymbol{J}_{nm} \hat{\boldsymbol{e}}_{nm}. \tag{21}$$

Here, $\hat{\boldsymbol{e}}_{nm}$ points from the atom at position $\boldsymbol{r}_n$ to its three nearest-neighbors $\boldsymbol{r}_m$ on each graphene sheet. In particular, the current amplitude is negligible at distances exceeding nearest-neighbor atoms and thus an average over nearest-neighbors is sufficient.

The spontaneously flowing currents of quasi-particles induce a magnetic field that can be calculated by applying the Biot-Savart law

$$\boldsymbol{B}(\boldsymbol{r}) = \frac{\mu_0}{4\pi} \int \boldsymbol{J}(\boldsymbol{r}) \times \frac{\boldsymbol{r} - \boldsymbol{r}'}{|\boldsymbol{r} - \boldsymbol{r}'|^3} d^3\boldsymbol{r}, \tag{22}$$

where μ_0 is the vacuum permeability. Since the current co-propagates in the two graphene sheets of TBG in the "chiral" phase, the magnetic fields induced by the supercurrents add constructively making this particular feature of the TRS breaking phase measurable in experiment.

[1] M. Koshino, N. F. Q. Yuan, T. Koretsune, M. Ochi, K. Kuroki, and L. Fu, Phys. Rev. X **8**, 031087 (2018).
[2] P. Moon and M. Koshino, Physical Review B **87**, 205404 (2013).
[3] J. L. Dos Santos, N. Peres, and A. C. Neto, Physical review B **86**, 155449 (2012).
[4] Z. Y. Rong and P. Kuiper, Phys. Rev. B **48**, 17427 (1993).
[5] K. Uchida, S. Furuya, J.-I. Iwata, and A. Oshiyama, Phys. Rev. B **90**, 155451 (2014).
[6] A. Sboychakov, A. Rakhmanov, A. Rozhkov, and F. Nori, Physical Review B **92**, 075402 (2015).
[7] L. Klebl and C. Honerkamp, Phys. Rev. B **100**, 155145 (2019).
[8] T. Ozaki, Phys. Rev. B **75**, 035123 (2007).
[9] S. L. Cunningham, Phys. Rev. B **10**, 4988 (1974).
[10] N. Berk and J. Schrieffer, Physical Review Letters **17**, 433 (1966).
[11] A. T. Rømer, S. Graser, T. S. Nunner, P. J. Hirschfeld, and B. M. Andersen, Phys. Rev. B **86**, 054507 (2012).
[12] J.-X. Zhu, Bogoliubov-de Gennes method and its applications, Vol. 924 (Springer, 2016).